A Study on the Optoelectronic Properties of Lead Chalcogenides Nanospheres Using a Combination of Experimental and Theoretical Approach

Nur Farha Shaafi[1], Saifful Kamaluddin Muzakir[1*], Mohd Fakhrul Zamani Kadir[2], Shujahadeen B. Aziz[3,4]

[1]Material Technology Programme, Faculty of Industrial Sciences and Technology, Universiti Malaysia Pahang, Lebuhraya Tun Razak, Gambang, Kuantan, 26300, Pahang, Malaysia
[2]Center of Foundation Studies in Science, University of Malaya, 50603 Kuala Lumpur, Malaysia
[3]Advanced Polymeric Materials Research Lab, Department of Physics, College of Science, University of Sulaimani, Qylasan Street, Sulaimani, 46001 Kurdistan Regional Government, Iraq
[4]Komar Research Center (KRC), Komar University of Science and Technology, Sulaimani, 46001, Kurdistan Regional Government, Iraq

Abstract

Various morphologies and cluster geometries of lead chalcogenides (PbX, X = S, Se, Te) have been studied in the size range of 2 - 200 nm. The nanosized PbX clusters that are smaller than their exciton Bohr radius would experience deviation of optoelectronic properties (bandgap and energy levels) in comparison to that of the bulk. The multi-exciton generation (MEG) could be resulted upon expansion of energy levels of the quantum confined PbX; would expedite their application in photovoltaic field. The MEG would favor the increment of photo-generated current and therefore an increment of efficiency (η) of a photovoltaic device could be expected. The characterization of the electronic and emitting states of the quantum confined PbX is however received less attention. This paper aims to validate realistic models of PbX and establish a correlation between the validated models with the experimentally fabricated PbXs based on their optical properties. The narrow bandgap PbX models i.e., $(PbS)_n$, $(PbSe)_n$ and $(PbTe)_n$; which n = 4 - 80 were evaluated as realistic models using geometry optimizations and harmonic frequency calculations at the level of B3LYP functional and lanl2dz basis set. The PbX thin films were fabricated using thermal evaporator at vacuum pressure of 1.0×10^{-5} Torr. A nanosphere morphology of the yielded PbXs was observed using Field Emission Scanning Electron Microscopy (FESEM). The realistic models of $(PbS)_{80}$, $(PbSe)_{30}$ and $(PbTe)_{50}$ were successfully established and validated as a basic building block of the fabricated thin film based on their crystal structure of the synthesized PbXs; supports the morphological observations made using FESEM.

Keywords: lead chalcogenides, thermal evaporator, density functional theory

Article Info

Received 26th December 2019
Accepted 5th February 2020
Published 1st April 2020
*Corresponding author: Saifful Kamaluddin Muzakir; email: saifful@ump.edu.my

ISSN: 1823-7010, eISSN: 2600-7444

Introduction

Quantum confined semiconducting materials have gained numerous attention due to their novel electronic and optical properties. The lead chalcogenides (PbX, which X = S, Se and Te) exhibit large exciton Bohr radius i.e., 5.01 nm (PbS), 13.1 nm (PbSe) and 24.8 nm (PbTe) [1]. Various synthesis and fabrication routes that yield various morphologies of PbXs with size smaller than their exciton Bohr radius have been explored [2, 3, 4, 5]. The expanded energy levels and band gap of a quantum confined semiconducting materials would lead to the ability to exhibit multi exciton generation (MEG) upon absorption of one photon ($E_{photon} > E_g$) [6]. The MEG has attracted researchers in the photovoltaic field which theoretically would increase the efficiency of a photovoltaic device exceeding ca. 60% [7].

In a quantum confined PbX, a ground state electron would be excited to a higher energy level upon absorption of photon with energy greater than its bandgap ($E_{photon} >> E_g$) e.g., electron excitation from the highest occupied molecular orbital (HOMO -0) to the lowest unoccupied molecular orbital (LUMO +1). The excited state electron then would undergo a relaxation to a lower energy level of LUMO +0 which releases excess energy in form of medium-wavelength photon e.g., visible light with $E_{photon} \geq E_g$. The emitted photon subsequently would be absorbed by a neighboring ground state electron. A secondary electron excitation would be initiated (e.g., HOMO -0 to LUMO +0). Generation of two excitons could be expected cumulatively upon absorption of one photon (figure 1).

A bulk phase PbX is however consists of continuous energy levels – known as energy bands. Upon absorption of photon ($E_{photon} >> E_g$), a ground state electron would undergo i.e., (i) excitation and (ii) relaxation mechanism. The mechanisms would favor an emission of long-wavelength photon in the infrared regime e.g., heat ($E_{photon} \leq E_g$). The energy of the yielded heat is insufficient to excite any neighboring ground state electron, therefore would be dissipated to the surroundings [8].

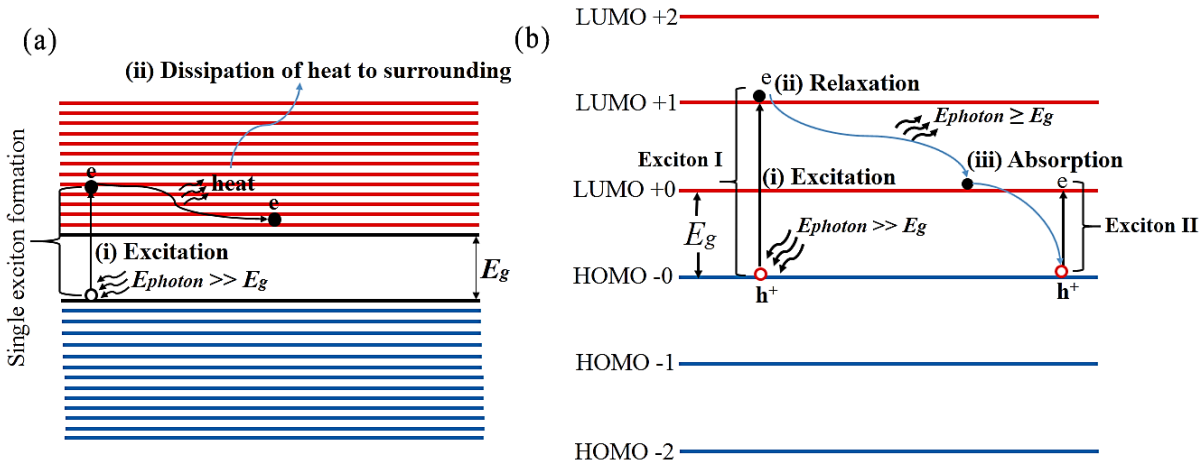

Figure 1: (a) Dissipation of excess energy of an excited state electron during relaxation to the lowest conduction band in bulk PbX. (b) The occurrence of MEG in quantum confined PbX upon absorption of one photon (E_{photon} >> E_g) which involves (i) excitation of a ground state electron, (ii) relaxation to the lowest unoccupied energy level with subsequent photon emission and (iii) absorption of photon by the neighboring electron and subsequent second electron excitation.

A drastic increment of publications in the field of photovoltaic using PbXs could be observed from 1970 to 2018 (figure 2); which is speculated due to the MEG. The PbXs exhibit narrow band gaps i.e., PbS (0.37 eV), PbSe (0.29 eV) and PbTe (0.29 eV); which could be tailored by size reduction of the basic building block of the PbXs below their exciton Bohr radius [9]. The PbXs are convenient for various applications i.e., (i) thermoelectric [10], (ii) infrared technologies (e.g., photoresistors, light-emitting diodes and lasers) [11], (iii) strain gauges [12], (iv) biological applications [13] and (v) photon absorbers [14].

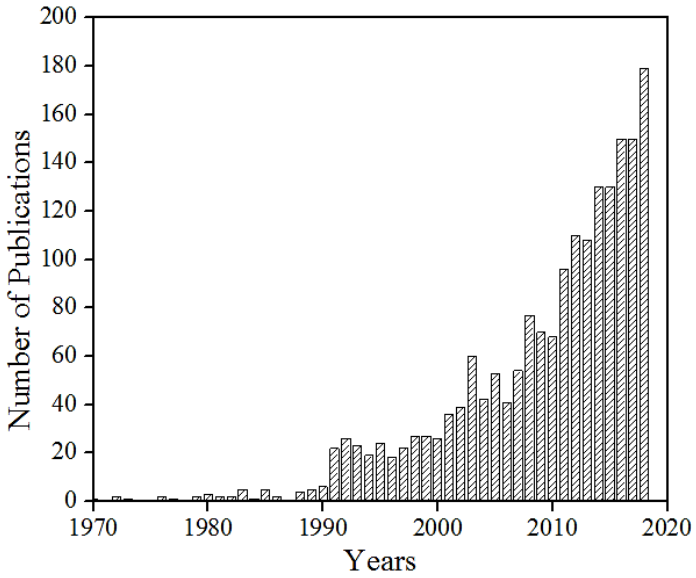

Figure 2: Number of papers published from 1970 to 2018; generated from ISI Web of Science using keywords 'lead chalcogenide'.

Quantum chemical calculations using functional of Becke's three parameter hybrid method Lee, Yang and Parr correlation functional (B3LYP) and basis set of Los Alamos

National Laboratory 2-double-z (lanl2dz) under the framework of density functional theory (DFT) could be utilized to simulate the PbX models [15]. The combination of functional and basis set would describe properties of materials i.e., (i) binding energy, (ii) trap states, (iii) surface states and (iv) surface stabilization [16,17,18,19] at high accuracy [20]. A gradual increase of DFT usage in photovoltaic research area could be observed in the number of publications from 2001 to 2018 (figure 3). The established realistic models have been used to study the occurrence of MEG from non-experimentally feasible perspectives i.e., (i) oscillator strength, (ii) optical absorptivity and (iii) excitation energy [21].

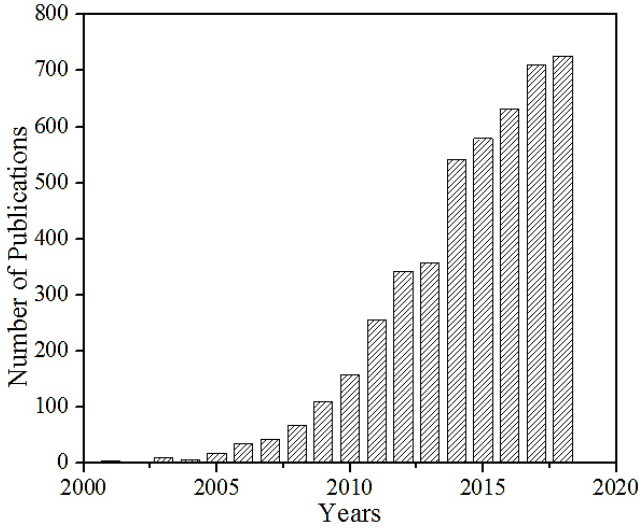

Figure 3: Number of papers published from 2001 to 2018; generated from ISI Web of Science using keywords 'density functional theory' and 'solar cell'

In this work, we aim to study the correlation between the optoelectronic properties of the realistic PbX models with that of the experimentally synthesized PbXs. The narrow bandgap PbX models i.e., $(PbS)_n$, $(PbSe)_n$ and $(PbTe)_n$ (which n = 4 – 80) were evaluated and validated as realistic models using geometry optimizations and harmonic frequency calculations at B3LYP/lanl2dz level of theory. The PbX thin films were fabricated using thermal evaporator at vacuum pressure of 1.0×10^{-5} Torr. The nanosphere morphology of the yielded PbXs was characterized using Field Emission Electron Microscope (FESEM), with Energy Dispersive X-Ray Spectrometer (EDX) and X-ray Diffractometer (XRD).

Materials and Methods

Materials

Materials used in this experiment were lead (II) sulfide (Sigma Aldrich; 99.9%), lead (II) selenide (Sigma Aldrich; 99.9%), lead (II) telluride (Sigma Aldrich; 99.9%) and conducting glass substrate (Kaivo indium tin oxide coated glass, transmittance of ca. 83%, resistance of ca. 10 Ω/cm^2).

Sample Preparations

The lead and chalcogenide reactants were mixed based on the molar ratio of 1:1 i.e., (i) Pb (0.21 g) and S (0.03 g), (ii) Pb (0.21 g) and Se (0.08 g) and (iii) Pb (0.21 g) and Te (0.13 g);

loaded into molybdenum boat. A conducting glass substrate is placed on the top of the boat (with distance ca. 5 cm from the boat). The lead chalcogenide thin films were fabricated using a thermal evaporator (Magna Value Thermal Evaporator; Model: TE MSSLAB/200) under an optimized environment to obtain a good adsorption of the film. The pressure of the chamber of thermal evaporator was set to 1.0×10^{-5} Torr using rotary pump. Different combinations of current and voltage were used i.e., (i) PbS (62 A, 1.27 V), (ii) PbSe (65 A, 1.53 V) and (iii) PbTe (67 A, 1.58 V). The deposited thin films on glass were cooled to room temperature.

Crystal structure of the thin films was investigated using Rigaku Miniflex II X-ray Diffractometer (Cu Kα source with X-ray wavelength of 1.5406 Å generated at 30 kV and 15 mA). A standardized scan range was set from 20° to 80°; with step width of 0.02°. The peak distortion by Kβ wavelength was hindered using a Nickel filter. The morphological study of the films was carried out using JEOL JSM 7800F FESEM. The absorption spectra of the films were plotted using Shimadzu UV-2600 spectrometer. The excitonic peaks were determined using graph fitting to four Gausssian peaks; which correspond to electronic transitions. The characteristic of radiative recombination of the excited state electron was studied using Edinburgh Instruments FS920 photoluminescence spectrometer.

Density Functional Theory Simulation

A few clusters of narrow bandgap lead chalcogenides i.e., (PbS)n, (PbSe)n and (PbTe)n (which n = 4, 6, 9, 12, 16, 30, 32, 40, 44, 50, 74 and 80) were modelled based on their crystallographic profiles. The models were the optimized to the lowest energy structure and evaluated as realistic models using harmonic frequency calculations at the level of B3LYP functional [22] and lanl2dz basis set. Models with optimized geometries which show positive frequencies of atomic vibrational modes were validated as realistic [23, 24]. Negative vibrational frequencies indicate non-realistic models; which the models were discarded. The optoelectronic properties of the realistic models i.e., (i) HOMO, (ii) LUMO and (iii) bandgap were calculated using time-dependent density functional theory (TDDFT). The size of the optimized models was calculated based on their molecular volume.

Results and Discussion

Crystal Structure Studies

The PbS, PbSe and PbTe thin films which comprise the PbX nanoclusters were successfully fabricated on the surface of conducting glass using thermal evaporator technique. The elemental composition in the thin films were verified using EDX spectroscopy (figure 4). The respective mass fraction in insets of figure 1 (a) – (c) showed that i.e., (i) Pb and S are 38.03% and 61.97%, (ii) Pb and Se are 72.60% and 27.40% and (iii) Pb and Te are 48.93% and 51.07%. The disproportionated elemental composition as indicated in the EDX spectra could be due to several factors i.e., (i) melting point (T_m) of Pb (327.5^{o}C), Se (220.0^{o}C) and Te (449.5^{o}C) which are higher than that of S (115.2^{o}C) [25, 26] and (ii) molecular weight (M_w) of Pb (207.2 g/mol) which is higher than that of the S (32.065 g/mol), Se (78.96 g/mol) and Te (127.6 g/mol) [27].

During the fabrication of PbS thin film (increment of temperature of molybdenum boat from room temperature to 1339^{o}C), the lead started to evaporate at temperature higher than 327.5^{o}C and adsorbed on the surface of the ITO. The sulphur however, reacted with

the molybdenum boat to form MoS_2 on the surface of the boat at the temperature (Δ_f) of 420ºC [28]. Upon increment of fabrication temperature (Δ_d), 1090ºC to 1339ºC [29], the MoS_2 dissociated and released sulphur which later adsorbed onto the surface of the ITO. The mechanism is depicted in equation (1) and (2); supports the observation made by the EDX analysis which showed high atomic % of sulphur on the surface of PbS thin film.

$$Mo_{(s)} + 2S_{(g)} \xrightarrow{\Delta f=420^{\circ}C} MoS_{2(s)} \quad (1)$$

$$MoS_{2(s)} \xrightarrow{\Delta d=1090^{\circ}C} Mo_{(s)} + 2S_{(g)} \quad (2)$$

The temperature of molybdenum boat was increased from room temperature to 1569ºC during the fabrication of PbSe thin film. The Se evaporated earlier and faster due to lower melting temperature and lower molecular weight than that of the Pb respectively. Therefore a Pb-rich surface of PbSe thin film is yielded.

The surface of the fabricated PbTe however showed ca. 1:1 atomic ratio due to simultaneous adsorption of Pb and Te onto the surface of the ITO. The Pb evaporated earlier, however with slower speed due to lower melting temperature and higher molecular weight than that of the Te. The Te evaporated later, however with faster speed due to high melting temperature and lower molecular weight than that of the Pb. Therefore, the Pb and Te adsorbed simultaneously onto the surface of ITO.

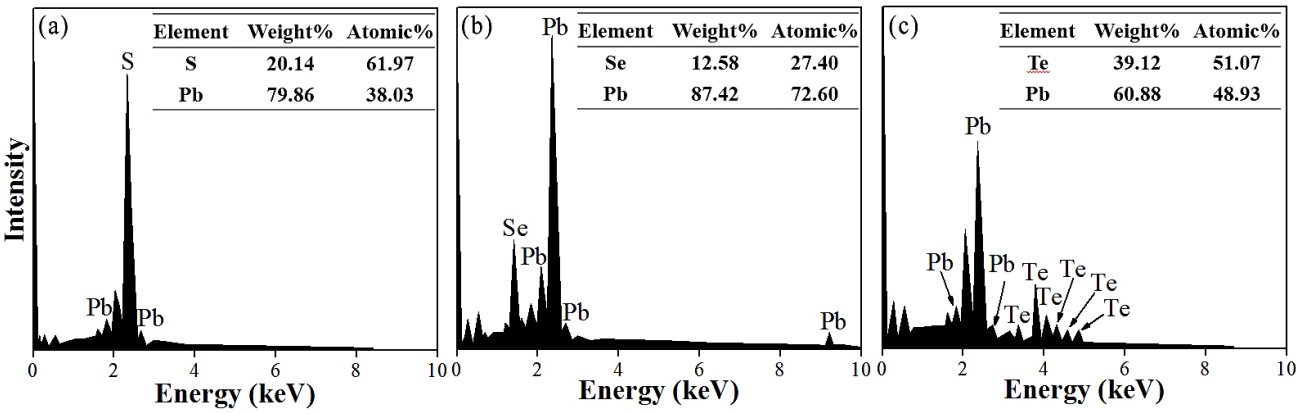

Figure 4: The EDX spectra and elemental analysis (inset) of the (a) PbS, (b) PbSe and (c) PbTe thin films.

The analysed XRD patterns of PbS, PbSe and PbTe thin films within the range of 10º – 80º (figure 5) revealed a halite (cubic) crystal structure. The respective distinct peaks were presented in PbS (at 2θ = 15.2º, 21.35º, 23.15º, 30.39º, 45.42º, 50.06º, 60.17º and 77.49º), PbSe (at 2θ = 24.99º, 29.02º, 41.59º, 50.50º, 59.99º, 68.2º and 76.0º) and PbTe (at 2θ = 23.51º, 27.99º, 39.84º, 47.02º, 49.17º, 57.36º, 64.83º and 72.03º) thin films; correspond to Miler indices of reflecting planes of i.e., (i) [101], [011], [111], [211], [203], [303], [511] and [333], (ii) [111], [200], [220], [311], [400], [331] and [422] crystal plane and (iii) [111], [200], [220], [311], [222], [400], [420] and [422] crystal planes. Additional peaks at 21.13º, 31.10º and 35.05º marked by "●" were identified to be in a good agreement with the peaks of the pre-deposited indium tin oxide (ITO) layer of the substrates (in all thin film samples); associated with planes [211], [222] and [400] respectively [30]. The

distinct sharp peaks of PbS thin film at 21.35° and 30.39° and PbTe thin film at 23.51° correspond to Miller indices of reflecting planes i.e., [011], [211] and [111] respectively, were overlapped with the ITO peaks and difficult to be discriminated.

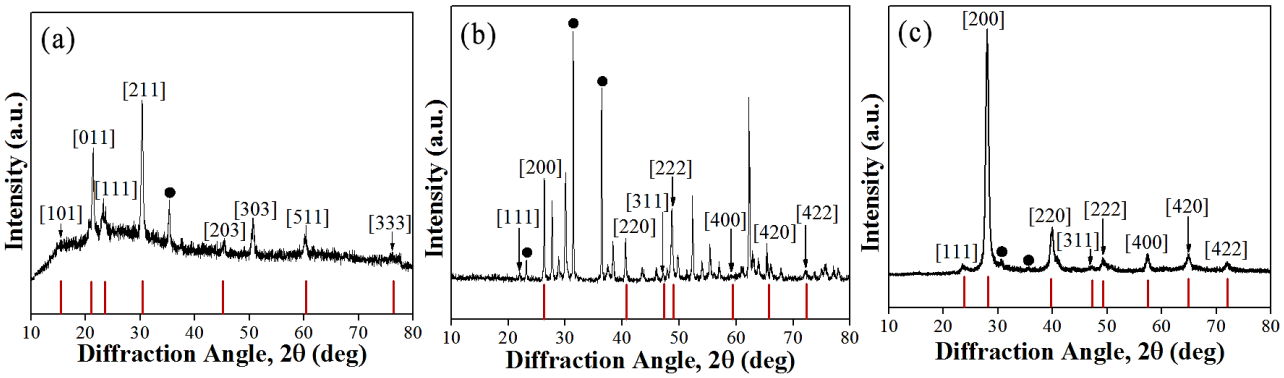

Figure 5: The XRD pattern of (a) PbS, (b) PbSe and (c) PbTe thin films.

Morphological Analysis

Nanosphere morphology (inset figure 6) of the PbS, PbSe and PbTe thin films were modelled based on the experimental XRD data; confirmed by the FESEM micrograph with size distributions i.e., (a) PbS (30-56 nm), (b) PbSe (35-69 nm) and (c) PbTe (28-65 nm) as depicted in figure 6 and 7. The PbS, PbSe and PbTe thin films with thickness of 0.71 µm, 0.52 µm and 0.91 µm respectively were measured in the cross-sectional view (figure 6 a (ii), b (ii) and c (ii)). In photovoltaic application, an electron would be excited from $HOMO_{PbX}$ to $LUMO_{PbX}$ upon absorption of photon with energy greater than their bandgap. The excited state electron later would be injected to the conduction band of photoelectrode. The excited state electron however, would travel from the PbX to the location which electronically in contact with the photoelectrode to ensure efficient injection, and therefore the electron-hole recombination could be prevented. The electron diffusion length (L_D) indicates the traveling distance of an excited state electron before a recombination would occur, depicted using the following equation (3):

$$L_D = L\sqrt{\tau_r/\tau_t} \tag{3}$$

where L is PbX electron transfer layer thickness, τ_r is an electron recombination lifetime and τ_t is an electron transport lifetime. The thickness of the fabricated thin films i.e., PbS (0.71 µm), PbSe (0.52 µm) and PbTe (0.91 µm) is smaller than the L_D of lead chalcogenides i.e., (i) PbS (3.90 µm) [31], (ii) PbSe (1.00 µm) [32], (iii) PbTe (1.7 µm) [33], therefore efficient electron injection from PbX to photoelectrode could be expected [34]. The realistic models of PbX were calculated using quantum chemical calculations based on the crystal structures and morphologies which elaborated in the next section.

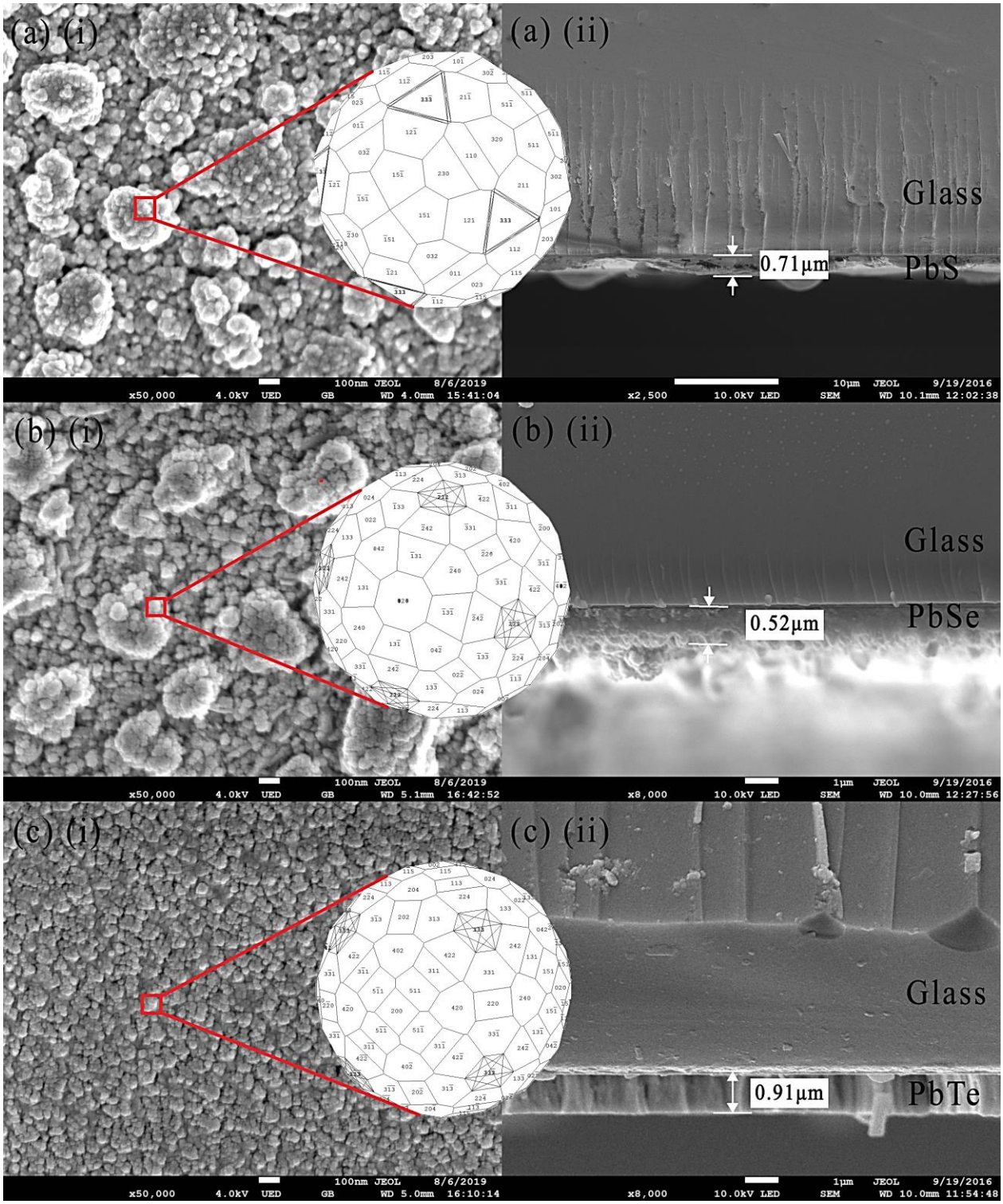

Figure 6: FESEM micrograph reveals that i.e., (a)(i) PbS (diameter range ca. 30-56 nm), (b)(i) PbSe (diameter range ca. 30-69 nm) and (c)(i) PbTe (diameter range ca. 28-65 nm) thin films consists of nanosphere particles. The cross section thin films showed the thickness of (a)(ii) PbS (0.71 µm), (b)(ii) PbSe (0.52 µm) and (c)(ii) PbTe (0.91 µm).

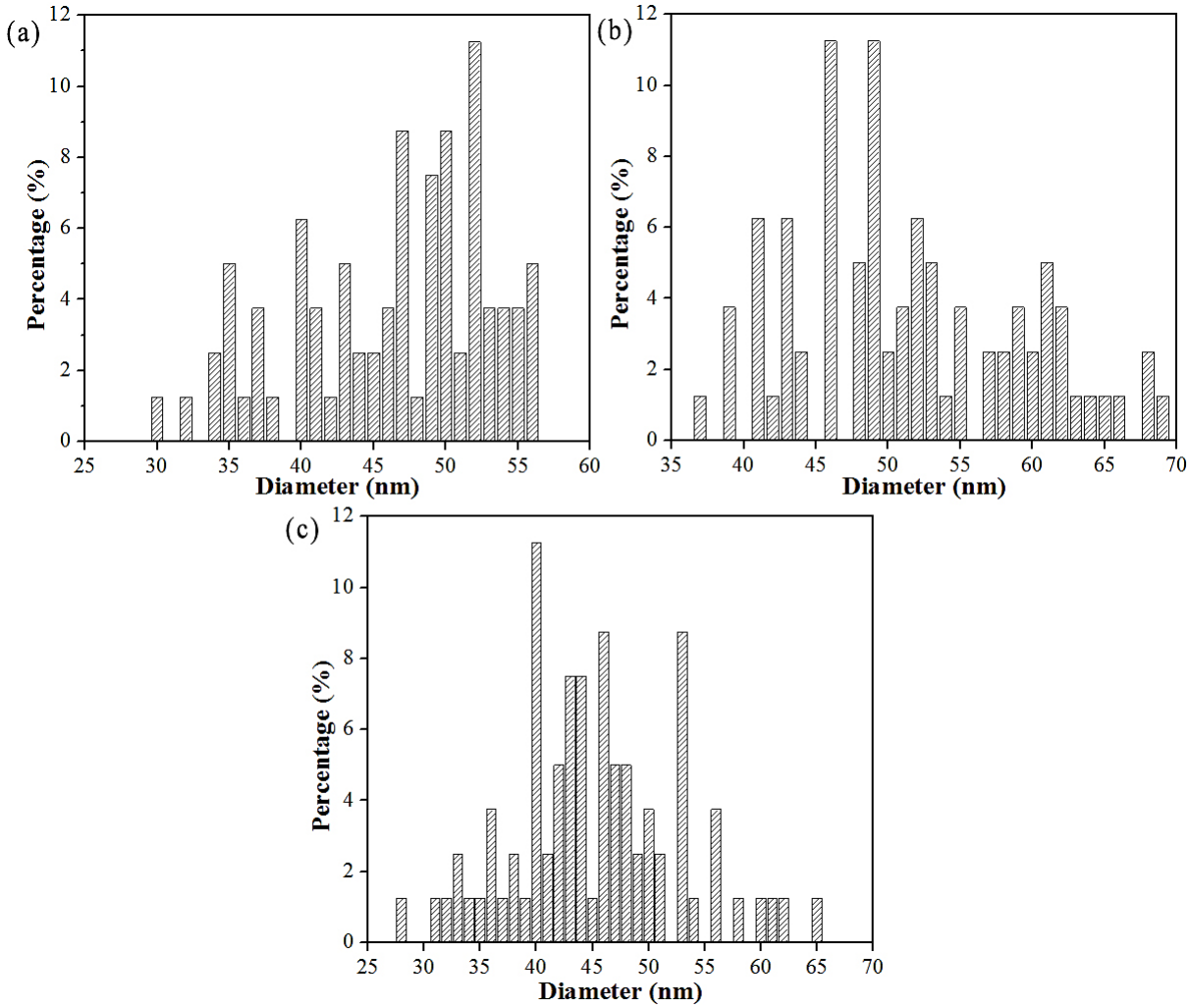

Figure 7: The size distributions of (a) PbS, (b) PbSe and (c) PbTe thin films.

Realistic PbX Cluster Modelling

Several PbS , PbSe and PbTe geometries have been optimized to the lowest energy structure (figure 8 and supplementary information, S1-S3), viz., $(PbS)_4$, $(PbS)_6$, $(PbS)_9$, $(PbS)_{12}$, $(PbS)_{16}$, $(PbS)_{30}$, $(PbS)_{40}$, $(PbS)_{74}$, $(PbS)_{80}$, $(PbSe)_4$, $(PbSe)_6$, $(PbSe)_{12}$, $(PbSe)_{16}$, $(PbSe)_{30}$, $(PbSe)_{32}$, $(PbSe)_{50}$, $(PbSe)_{74}$, $(PbTe)_4$, $(PbTe)_6$, $(PbTe)_9$, $(PbTe)_{12}$, $(PbTe)_{16}$, $(PbTe)_{44}$, $(PbTe)_{50}$ and $(PbTe)_{74}$. The subscripts denote the number of atoms in the optimized models [35, 36, 37]. The lead chalcogenides were modelled based on crystal properties which determined by the XRD i.e., space group, bond lengths, bond angles and dihedral angles. The size of $(PbS)_{80}$, $(PbSe)_{30}$ and $(PbTe)_{50}$ clusters i.e., 4.58 nm, 3.48 nm and 4.24 nm respectively, were calculated based on their volume; smaller than their exciton Bohr radius i.e., 5.01, 13.1 and 24.8 nm respectively [38]. This observation therefore heading to a conclusion that the models are in a strong quantum confinement region, which the geometry, optical, electronic properties of the clusters would be deviated from that of the bulk.

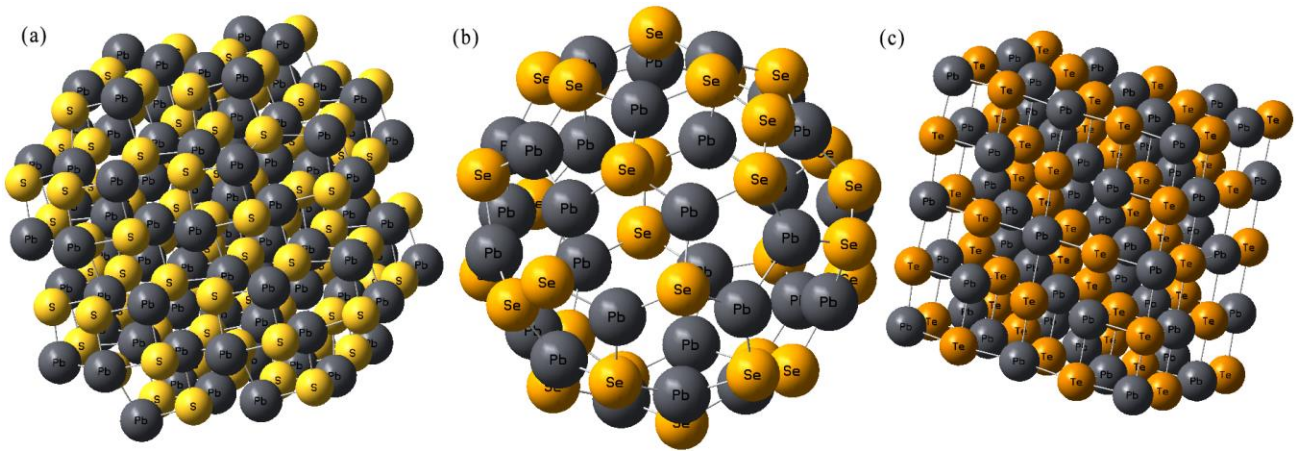

Figure 8: Optimized geometries of (a) $(PbS)_{80}$, (b) $(PbSe)_{30}$ and (c) $(PbTe)_{50}$.

Optical Properties Analysis

The optical properties of the PbS, PbSe and PbTe thin films were analyzed using absorption spectrometer (figure. 9a, 9c, 9e) and compared with that of the theoretically calculated absorption spectra (figure 9b, 9d, 9f). The absorption spectra were carefully fitted to four Gaussian peaks which correspond to the first, second, third and fourth excitonic peaks (Table 1). The first excitonic peak of the thin films and theoretical models were further investigated, revealed that the first excitonic peak of $(PbS)_{80}$, $(PbSe)_{30}$ and $(PbTe)_{50}$ clusters are in a good agreement with that of the experimentally characterized thin film.

In a bare lead chalcogenide, an electron would be excited upon absorption of single photon with sufficient energy ($E_{photon} >> E_g$) from the highest occupied molecular orbital (HOMO) to the lowest unoccupied molecular orbital (LUMO), leaving a hole (electron vacancy) in the HOMO. Subsequent radiative recombination could be expected from the $LUMO_{PbX}$ to the $HOMO_{PbX}$ and the photon emission could be observed using Photoluminescence (PL) spectrometer.

The bond lengths, bond angles and dihedral angles in crystal structures smaller than their exciton Bohr radius would deviate from that of in the bulk phase, which indicate the occurrence of surface distortion [39]. The deviated structures would provide trap states of lower energies than that of $LUMO_{PbX}$, therefore, would result a broad PL emission. The higher the percentage of deviation, therefore the deeper the trap states would be. Furthermore, the existence of trap states in between the $LUMO_{PbX}$ and the $HOMO_{PbX}$ would favor non-radiative electron injections from the $LUMO_{PbX}$ to the trap states, which undetectable by the PL spectrometer – therefore consequently would lower the cumulative PL intensity. The recombination behavior showed that the PL intensity of the bulk PbX ($\times 10^5$ counts) are higher than that of the PbX thin films ($\times 10^4$ counts), as depicted in figure 10. Nonetheless, the PbX thin films showed broad PL peaks, which correspond to electron recombination from trap states to the $HOMO_{PbX}$.

The PbX thin films are targeted to be used as fluorophore in photovoltaic applications. The ability of the fluorophore to conserve the energy of the highly energized excited state electrons during electron injections from the fluorophore to the photoelectrode e.g., metal oxide semiconductor (MOS), needs to be discussed systematically [40]. Energy loss could be expected due to existence of the surface traps with energy in between the $LUMO_{PbX}$ and $HOMO_{PbX}$. The surface traps would lead to unnecessary non-radiative

electron injection from $LUMO_{PbX}$ to trap states and thereby lower the probability of electron injection from the $LUMO_{PbX}$ to $LUMO_{MOS}$. The PbS, PbSe and PbTe showed large Stoke's shift i.e., 284 nm, 268 nm and 111 nm respectively (figure 11(a), (c), (e)), could be correlated to the existence of the deep trap states [41, 42, 43], resulted from irregular surface of small-sized PbS (4.58 nm), PbSe (3.48 nm) and PbTe (4.24 nm) respectively. The Stoke's shifts were recalculated based on the established realistic models, which revealed increasing trend of deviation percentage of 67.13%, 46.58% and 30.00% from that of the experimental-based calculations, with the increment of molecular weight i.e., PbS (239.30 g/mol), PbSe (286.16 g/mol) and PbTe (334.80 g/mol) respectively (figure 8(b), (d), (f)). Significant energy loss is expected i.e., 0.67 eV, 0.46 eV and 0.30 eV in the fabricated PbS, PbSe and PbTe thin films respectively, based on the experimentally characterized Stoke's shift.

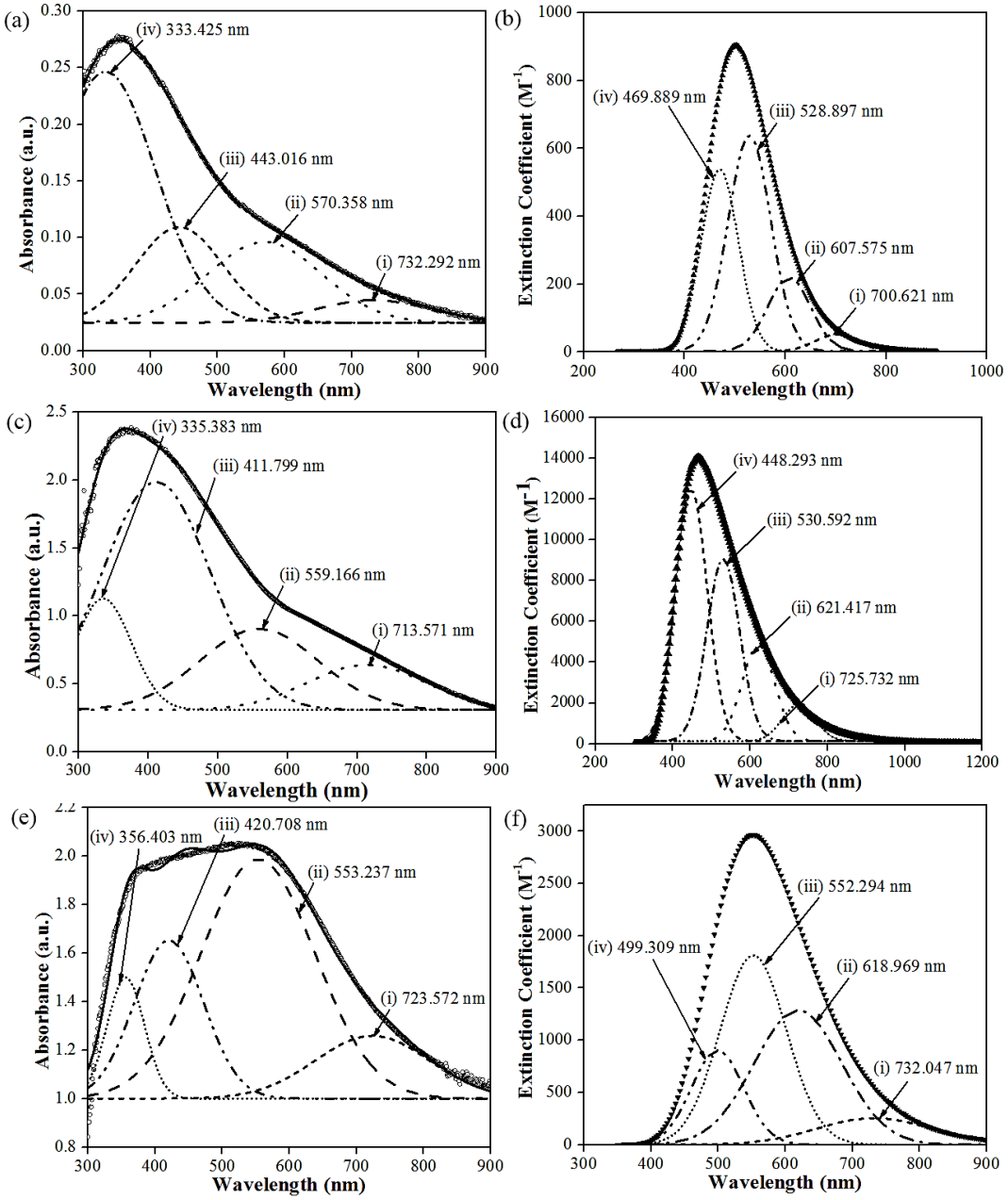

Figure 9: The excitonic peaks of (a) PbS thin film, (b) $(PbS)_{80}$ realistic model, (c) PbSe thin film, (d) $(PbSe)_{30}$ realistic model, (e) PbTe thin film and (f) $(PbTe)_{50}$ realistic model; fitted to four Gaussian peaks.

Table 1: Positions of excitonic peaks of the PbX thin film and realistic models.

(a)	PbS	Excitonic peak position (wavelength)			
		1st(nm)	2nd(nm)	3rd(nm)	4th (nm)
	Thin Film	732.292	570.358	443.016	333.425
	$(PbS)_4$	379.784	306.481	283.898	268.616
	$(PbS)_6$	386.397	350.119	320.481	296.621
	$(PbS)_9$	449.869	403.932	371.970	342.319
	$(PbS)_{12}$	370.872	327.089	305.151	283.814
	$(PbS)_{16}$	383.545	350.774	326.605	306.775
	$(PbS)_{30}$	460.429	413.628	379.025	350.600
	$(PbS)_{40}$	583.676	519.813	472.603	432.886
	$(PbS)_{74}$	810.878	683.314	612.247	539.960
	$(PbS)_{80}$	700.621	607.575	528.897	469.889

(b)	PbSe	Excitonic peak position (wavelength)			
		1st(nm)	2nd(nm)	3rd(nm)	4th (nm)
	Thin Film	713.571	559.166	411.799	335.383
	$(PbSe)_4$	471.250	421.898	321.744	309.959
	$(PbSe)_6$	445.913	398.045	360.657	328.354
	$(PbSe)_{12}$	405.785	360.676	332.457	306.957
	$(PbSe)_{16}$	636.252	504.311	442.777	402.942
	$(PbSe)_{30}$	725.732	621.417	530.592	448.293
	$(PbSe)_{32}$	611.784	545.404	495.202	452.746
	$(PbSe)_{50}$	747.119	652.180	574.159	506.757
	$(PbSe)_{74}$	820.834	708.907	631.881	560.498

(c)	PbTe	Excitonic peak position (wavelength)			
		1st(nm)	2nd(nm)	3rd(nm)	4th (nm)
	Thin Film	723.572	553.237	420.708	356.403
	$(PbTe)_4$	553.225	480.060	386.568	358.619
	$(PbTe)_6$	582.217	512.973	442.851	395.037
	$(PbTe)_9$	662.163	556.199	489.760	436.178
	$(PbTe)_{12}$	629.049	525.393	435.421	384.398
	$(PbTe)_{16}$	478.534	422.126	363.421	332.147
	$(PbTe)_{44}$	880.233	693.901	602.310	535.731
	$(PbTe)_{50}$	732.047	618.969	552.294	499.309
	$(PbTe)_{74}$	1068.026	871.949	714.127	616.029

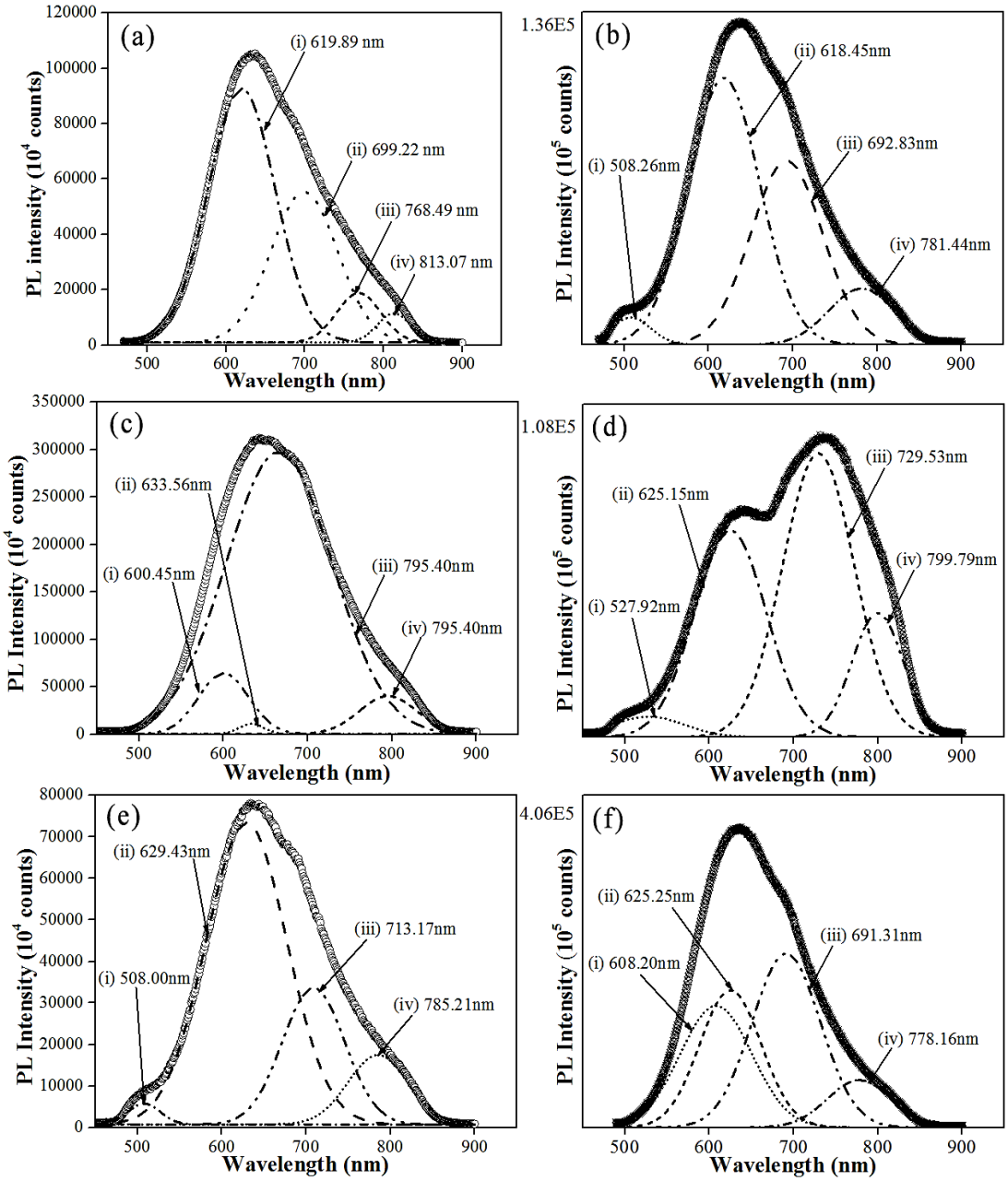

Figure 10: The PL peaks of (a) PbS thin film, (b) PbS bulk, (c) PbSe thin film, (d) PbSe bulk, (e) PbTe thin film and (f) PbTe bulk; fitted to four Gaussian peaks.

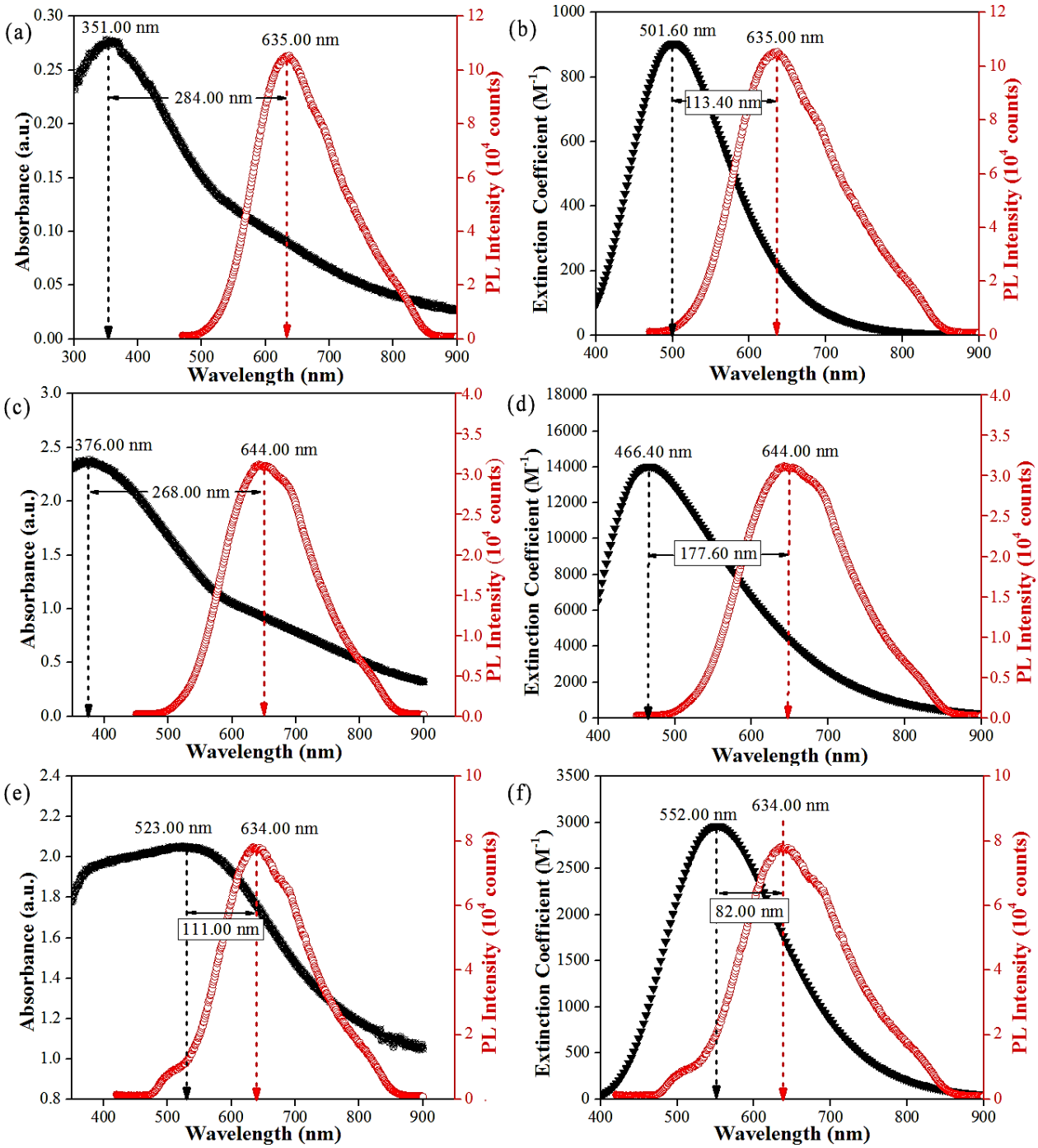

Figure 11: A comparison between the Stoke's shift calculated based on experimentally-characterized absorption and photoluminescence spectra of (a) PbS, (c) PbSe and (e) PbTe thin films (left hand side), with the Stoke's shift calculated based on theoretically-calculated absorption spectra and experimentally-characterized photoluminescence spectra of (b) PbS, (d) PbSe and (f) PbTe realistic models (right hand side).

Conclusions

In conclusion, a comparative study between experimental and theoretical works employing quantum chemical calculations has been carried out, and revealed a correlation of optoelectronic properties of fabricated PbS, PbSe and PbTe thin films with that of the theoretical analogues. The PbX thin films were fabricated using thermal evaporator at particular parameters i.e., voltage, current and pressure which have been mentioned in the earlier section. The realistic models of $(PbS)_{80}$, $(PbSe)_{30}$ and $(PbTe)_{50}$ are hypothesized could be the basic building block of the nanospheres as observed under the FESEM. The size distributions of the nanospheres are in the range of i.e., (i) PbS (ca. 30-56 nm), (ii) PbSe (ca. 30-69 nm) and (iii) PbTe (ca. 28-65 nm). Several observations have been discussed which correlates the properties of the fabricated thin films with that of the theoretically determined models i.e., (i) PbX with the size of i.e., PbS (4.58 nm), PbSe (3.48 nm) and PbTe (4.24 nm) were validated as realistic models, revealed that the first excitonic peaks are in a good agreement with that of the experimentally characterized thin film, (ii) decrement of PL intensity could be due to the existence of deep and shallow trap states, which correlated to irregular surfaces of small PbX clusters and (iii) significant energy loss could be expected before an electron injections could happen from the PbX thin films to photoelectrode - would jeopardize the efficiency of a photovoltaic devices. Therefore optimized fabrication parameters that would yield thin films with low number of trap states should be targeted.

Acknowledgements

This work is funded by the Research & Innovation Department of Universiti Malaysia Pahang and the Ministry of Education of Malaysia through the Fundamental Research Grant Scheme (RDU 150111) and Postgraduate Research Scheme (PGRS190346).

Author Contributions

All authors contributed toward data analysis, drafting and critically revising the paper and agree to be accounted for all aspects of the work.

Disclosure of Conflict of Interest

The authors have no disclosures to declare.

Compliance with Ethical Standards

The work is compliant with ethical standards.

References

[1] Ma, W., Luther, J. M., Zheng, H., Wu, Y., & Alivisatos, A. P. (2009). *Nano. Lett.* 9(4), 1699-1703.

[2] Chen, D., & Chen, X. (2019). Luminescent perovskite quantum dots: synthesis, microstructures, optical properties and applications. *Journal of Materials Chemistry C*, *7*(6), 1413-1446.

[3] Kulkarni, S. A., Mhaisalkar, S. G., Mathews, N., & Boix, P. P. (2019). Perovskite Nanoparticles: Synthesis, Properties, and Novel Applications in Photovoltaics and LEDs. *Small Methods*, *3*(1), 1800231.
[4] Shamsi, J., Urban, A. S., Imran, M., De Trizio, L., & Manna, L. (2019). Metal halide perovskite nanocrystals: synthesis, post-synthesis modifications, and their optical properties. *Chemical reviews*, *119*(5), 3296-3348.
[5] Polavarapu, L., Nickel, B., Feldmann, J., & Urban, A. S. (2017). Advances in Quantum-Confined Perovskite Nanocrystals for Optoelectronics. *Advanced Energy Materials*, *7*(16), 1700267.
[6] Ellingson, R. J., Beard, M. C., Johnson, J. C., Yu, P., Micic, O. I., Nozik, A. J., & Efros, A. L. (2005). Highly Efficient Multiple Exciton Generation in Colloidal PbSe And PbS Quantum Dots. *Nano letters*, *5*(5), 865-871.
[7] Murphy, J. E., Beard, M. C., Norman, A.G., Ahrenkiel, S. P., Johnson, J.C., Yu, P., Micic, O. I., Ellingson, R. J. & Nozik, A. J. (2006). *J. Am. Chem. Soc*.
[8] Murphy, J. E., Beard, M. C., Norman, A. G., Ahrenkiel, S. P., Johnson, J. C., Yu, P., & Nozik, A. J. (2006). PbTe Colloidal Nanocrystals: Synthesis, Characterization, and Multiple Exciton Generation. *ACS Chem*. 128(10), 3241-3247.
[9] Yan, L., Shen, X., Zhang, Y., Zhang, T., Zhang, X., Feng, Y. & William, W. Y. (2015). Near-infrared Light Emitting Diodes Using Pbse Quantum Dots. *RSC Advances*. *5*(67), 54109-54114.
[10] Cao, H., Wang, G., Zhang, S., & Zhang, X. (2006). Growth and photoluminescence properties of PbS Nanocubes. *Nanotechnology*. *17*(13), 3280.
[11] Kane, R. S., Cohen, R. E., & Silbey, R. (1996). Theoretical study of the electronic structure of PbS Nanoclusters. *J. Phys. Chem. A*. *100*(19), 7928-7932.
[12] Ravich, I. I. (2013). Semiconducting Lead Chalcogenides (Vol. 5). *Springer Science & Business Media*.
[13] Khokhlov, D. (2002). Lead Chalcogenides: Physics and Applications. *CRC Press*.
[14] Hirata, H., & Higashiyama, K. (1971). Analytical Study of the Lead Ion-Selective Ceramic Membrane Electrode. *Bulletin of the chemical society of Japan*. *44*(9), 2420-2423.
[15] Shaafi, N. F., Muzakir, S. K., & Sahraoui, B. (2019). A Study of the Electron Regeneration Efficiency of Solar Cells Fabricated Using CMC/PVA-, Alginate-, and Xanthan-based Electrolytes. *Makara Journal of Technology*, *23*(2), 53-58.
[16] Muzakir, S. K., Alias, N., Yusoff, M. M., & Jose, R. (2013). On the Missing Links In Quantum Dot Solar Cells: A DFT Study On Fluorophore Oxidation And Reduction Processes in Sensitized Solar Cells. *Phys. Chem. Chem. Phys*. *15*(38), 16275-16285.
[17] Fischer, S. A., Crotty, A. M., Kilina, S. V., Ivanov, S. A., & Tretiak, S. (2012). Passivating Ligand and Solvent Contributions to the Electronic Properties of Semiconductor Nanocrystals. *Nanoscale*. *4*(3), 904-914.
[18] Koch, W., & Holthausen, M. C. (2015). A Chemist's Guide to Density Functional Theory. *John Wiley & Sons*.
[19] Muzakir, S. K., & Jose, R. Identification of $(CdSe)_{32}$ Structure in Microemulsion-Based Synthesis.
[20] Argeri, M., Fraccarollo, A., Grassi, F., Marchese, L., & Cossi, M. (2011). Density Functional Theory Modeling of PbSe Nanoclusters: Effect of Surface Passivation on Shape and Composition. *J. Phys. Chem. C*. 115(23), 11382-11389.
[21] Gordi, M., Moravvej-Farshi, M. K., & Ramezani, H. (2018). Effects of Electric Fields on Multiple Exciton Generation. *Chem. Phys. Chem*. 19(20), 2782-2787.
[22] Yang, Y., Li, J., Wu, H., Oh, E., & Yu, D. (2012). Controlled ambipolar doping and gate voltage dependent carrier diffusion length in lead sulfide nanowires. *Nano letters*, *12*(11), 5890-5896.

[23] Zhuiykov, S. (2018). *Nanostructured Semiconductors*. Woodhead Publishing.
[24] Shufer, E., Dashevsky, Z., Kasiyan, V., Flitsiyan, E., Chernyak, L., & Gartsman, K. (2010). Electrical conductivity and minority carrier diffusion in thermally oxidized PbTe thin films. *Physica B: Condensed Matter*, *405*(4), 1058-1061.
[25] Lee, C., Yang, W., & Parr, R. G. (1988). Development of the Colle-Salvetti Conelation Energy Formula into A Functional Of The Electron Density. *Phys. Rev. vol. B*. 37, 785-789.
[26] Muzakir, S. K., Alias, N., Yusoff, M. M., & Jose, R. (2013). On the missing links in quantum dot solar cells: a DFT study on fluorophore oxidation and reduction processes in sensitized solar cells. *Physical Chemistry Chemical Physics*, *15*(38), 16275-16285.
[27] Jose, R., Zhanpeisov, N. U., Fukumura, H., Baba, Y., & Ishikawa, M. (2006). Structure− property correlation of CdSe clusters using experimental results and first-principles DFT calculations. *Journal of the American Chemical Society*, *128*(2), 629-636.
[28] Dutrizac, J. E. (1970). The reaction of sulphur vapour with molybdenum metal. *Canadian Metallurgical Quarterly*, *9*(3), 449-453.
[29] Brainard, W. A. (1968). *The Thermal Stability and Friction of the Disulfides, Diselenides, and Ditellurides of Molybdenum and Tungsten in Vacuum (10⁹ to 10⁶ Torr)*. National Aeronautics and Space Administration.
[30] Cverna, F. (Ed.). (2002). ASM Ready Reference: Thermal Properties of Metals. *ASM International*.
[31] Meyer, B. (1976). Elemental Sulfur. *Chem. Rev*. 76(3), 367-388.
[32] Francis, L. F. (2015). Materials Processing: A Unified Approach to Processing of Metals, Ceramics and Polymers. *Academic Press.*
[33] Vieira, N. C. S., Fernandes, E. G. R., Queiroz, A. A. A. D., Guimarães, F. E. G., & Zucolotto, V. (2013). Indium Tin Oxide Synthesized by A Low Cost Route as SEGFET pH Sensor. *Mat. Res.* 16(5), 1156-1160.
[34] Li, D., Jiang, Z., Xia, Q., & Yao, Z. (2019). Pre-or post-TiCl4 treated TiO2 nano-array photoanode for QDSSC: Ti3+ self-doping, flat-band level and electron diffusion length. *Applied Surface Science*, *491*, 319-327.
[35] Skums V.F., Pink R.L., & Allasov M.R. (1991). Solid Solutions of the PbSe - PbS System at High Pressures, Inorganic Materials (USSR) (see: Izv.Akad.Nauk, Neorg.Mater.). 27, 1336-1340.
[36] Mariano A.N., & Chopra K.L. Polymorphism in Some IV-VI Compounds Induced by High Pressure And Thin-Film Epitaxial Growth. *Appl. Phys. Lett.* 10 (1967) 282-284.
[37] Krebs, H., Green, K., & Kallen, D. (1961). About Structure and Properties of Semi-Metals. XIV. Mixed-Crystal Systems Between Semiconducting Chalcogenides of the Fourth Main Group. *Int. J. Inorg. Chem*. 312 (5-6), 307-313.
[38] Ma, W., Luther, J. M., Zheng, H., Wu, Y., & Alivisatos, A. P. (2009). Photovoltaic Devices Employing Ternary PbS X Se1-X Nanocrystals. *Nano lett*. 9(4), 1699-1703.
[39] Landes, C. F., Braun, M., & El-Sayed, M. A. (2001). On The Nanoparticle to Molecular Size Transition: Fluorescence Quenching Studies. *J. Phys. Chem. B*. 105(43), 10554-10558.
[40] Eychmüller, A., Hässelbarth, A., Katsikas, L., & Weller, H. (1991). Photochemistry of Semiconductor Colloids. Fluorescence Investigations on the Nature of Electron and Hole Traps in Q-Sized Colloidal CdS Particles. *Berichte der Bunsengesellschaft für physikalische Chemie*. 95(1), 79-84.
[41] Spanhel, L., Haase, M., Weller, H., & Henglein, A. (1987). Photochemistry of Colloidal Semiconductors. 20. Surface Modification and Stability of Strong Luminescing CdS Particles. *ACS.* 109(19), 5649-5655.

[42] Bawendi, M. G., Wilson, W. L., Rothberg, L., Carroll, P. J., Jedju, T. M., Steigerwald, M. L., & Brus, L. E. (1990). Electronic Structure and Photoexcited-Carrier Dynamics in Nanometer-Size CdSe Clusters. *Phys. Rev. Lett.* 65(13), 1623.
[43] Wang, Y. R., & Duke, C. B. (1988). Cleavage Faces of Wurtzite CdS and CdSe: Surface Relaxation and Electronic Structure. *Phys. Rev. B.* 37(11), 6417.

Supplementary Information

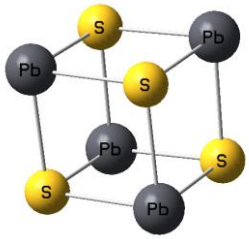

$(PbS)_4$

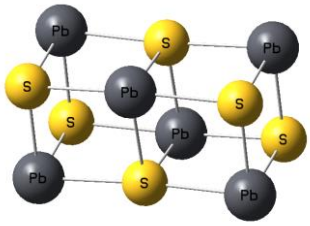

$(PbS)_6$

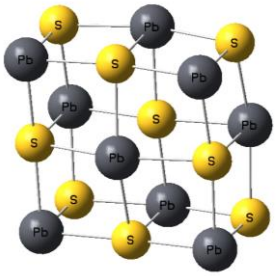

$(PbS)_9$

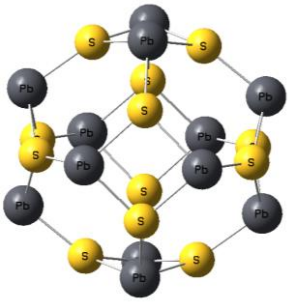

$(PbS)_{12}$

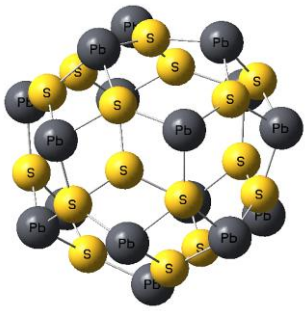

$(PbS)_{16}$

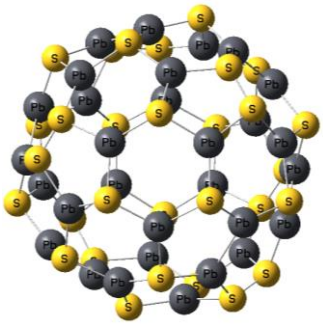

$(PbS)_{30}$

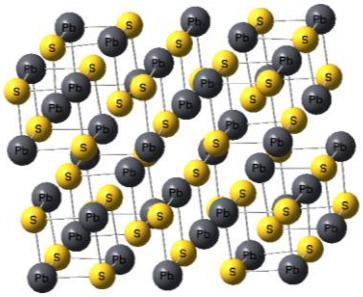

$(PbS)_{40}$

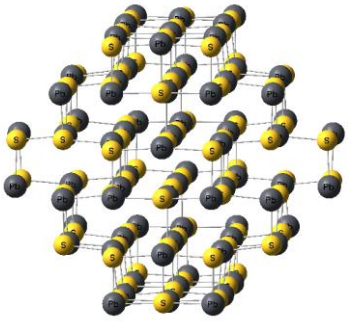

$(PbS)_{74}$

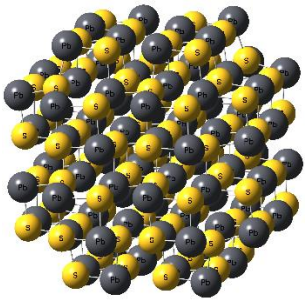

$(PbS)_{80}$

Supplementary 1: Optimized geometries of PbS i.e., $(PbS)_4$, $(PbS)_6$, $(PbS)_9$, $(PbS)_{12}$, $(PbS)_{16}$, $(PbS)_{30}$, $(PbS)_{40}$, $(PbS)_{74}$ and $(PbS)_{80}$.

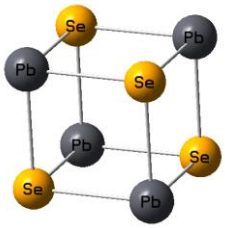

$(PbSe)_4$

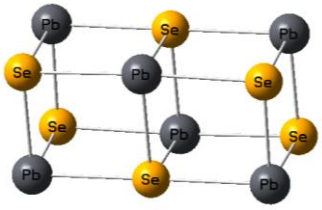

$(PbSe)_6$

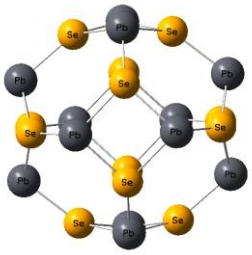

$(PbSe)_{12}$

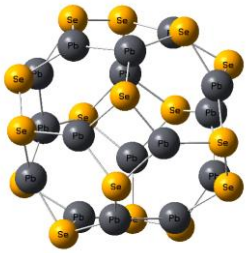

$(PbSe)_{16}$

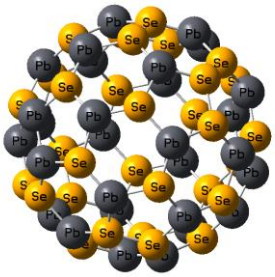

$(PbSe)_{30}$

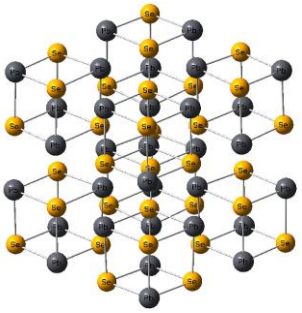

$(PbSe)_{32}$

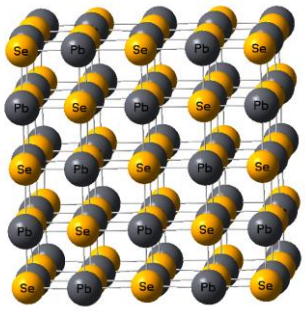

$(PbSe)_{50}$

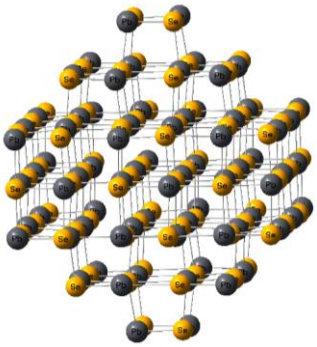

$(PbSe)_{74}$

Supplementary 2: Optimized geometries of PbSe i.e., $(PbSe)_4$, $(PbSe)_6$, $(PbSe)_{12}$, $(PbSe)_{16}$, $(PbSe)_{30}$, $(PbSe)_{32}$, $(PbSe)_{50}$ and $(PbSe)_{74}$.

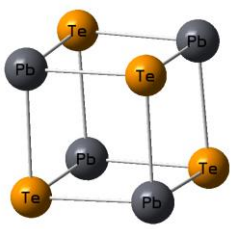

$(PbTe)_4$

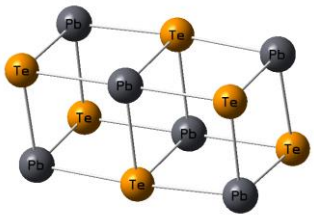

$(PbTe)_6$

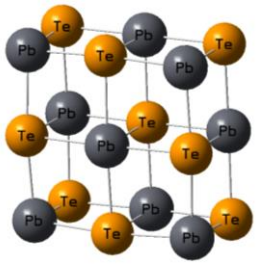

$(PbTe)_9$

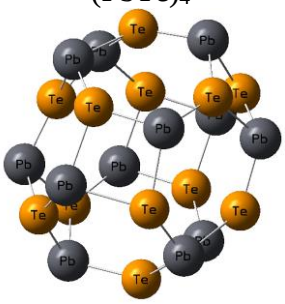

$(PbTe)_{12}$

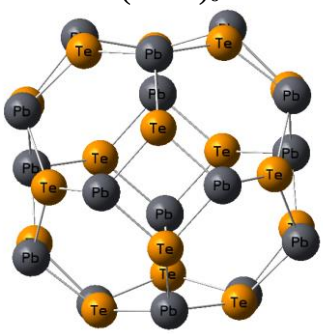

$(PbTe)_{16}$

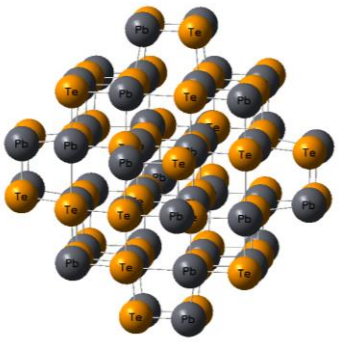

$(PbTe)_{44}$

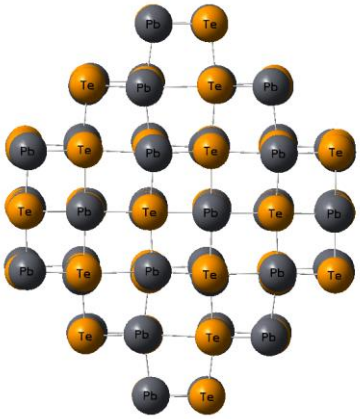

$(PbTe)_{74}$

Supplementary 3: Optimized geometries of PbTe i.e., $(PbTe)_4$, $(PbTe)_6$, $(PbTe)_9$, $(PbTe)_{12}$, $(PbTe)_{16}$, $(PbTe)_{44}$ and $(PbTe)_{74}$.